

# ImmunoPET Imaging of Multiple Myeloma with [<sup>68</sup>Ga]Ga-NOTA-Nb1053

**Cheng Wang**

Shanghai Jiao Tong University

**Yumei Chen**

Shanghai Jiaotong University Pao Yue Kong Library: Shanghai Jiao Tong University

**Yun Nan Hou**

Peking University Shenzhen Graduate School

**Qiufang Liu**

Fudan University Shanghai Cancer Center

**Di Zhang**

Shanghai Jiaotong University Pao Yue Kong Library: Shanghai Jiao Tong University

**Haitao Zhao**

Shanghai Jiaotong University Pao Yue Kong Library: Shanghai Jiao Tong University

**You Zhang**

Shanghai Jiao Tong University

**Shuxian An**

Shanghai Jiaotong University Pao Yue Kong Library: Shanghai Jiao Tong University

**Lianghua Li**

Shanghai Jiao Tong University

**Jian Hou**

Shanghai Jiao Tong University

**Gang Huang**

Shanghai Jiao Tong University

**Jianjun Liu**

Shanghai Jiao Tong University

**Yong Juan Zhao**

The Chinese University of Hong Kong

**Weijun Wei** (✉ [weijun.wei@outlook.com](mailto:weijun.wei@outlook.com))

Shanghai Jiao Tong University <https://orcid.org/0000-0003-3190-2480>

---

**Original Article**

**Keywords:** ImmunoPET, Multiple myeloma, Nanobody, CD38, Daratumumab

**Posted Date:** February 1st, 2021

**DOI:** <https://doi.org/10.21203/rs.3.rs-188294/v1>

**License:**  This work is licensed under a Creative Commons Attribution 4.0 International License.

[Read Full License](#)

---

**Version of Record:** A version of this preprint was published at European Journal of Nuclear Medicine and Molecular Imaging on February 5th, 2021. See the published version at <https://doi.org/10.1007/s00259-021-05218-1>.

# Abstract

**Purpose** Multiple myeloma (MM) remains incurable and its diagnosis relies heavily on bone marrow aspiration and biopsy. CD38 is a glycoprotein highly specific for MM. Antibody therapeutics (e.g., daratumumab) targeting CD38 have shown encouraging efficacy in treating MM, either as a monotherapy agent or in combination with other regimens. However, efficient stratification of patients who might benefit from daratumumab therapy and timely monitoring of the therapeutic responses are still clinical challenges. This work aims to devise a CD38-targeted imaging strategy and assess its value in diagnosing MMs.

**Methods** By labeling a CD38-specific single domain antibody (Nb1053) with  $^{68}\text{Ga}$  ( $t_{1/2} = 1.1$  h), we developed a CD38-targeted immuno-positron emission tomography (immunoPET) imaging probe [ $^{68}\text{Ga}$ ]Ga-NOTA-Nb1053. The probe was developed with good radiochemical yield (> 50%), excellent radiochemical purity (> 99%), and immunoreactivity (> 95%). The diagnostic accuracy of the probe was thoroughly investigated in preclinical MM models.

**Results** ImmunoPET imaging with the probe specifically depicted all the subcutaneous and orthotopic MM lesions, outperforming the traditional  $^{18}\text{F}$ -fluorodeoxyglucose PET and the nonspecific [ $^{68}\text{Ga}$ ]Ga-NOTA-NbGFP immunoPET. More importantly, daratumumab preloading significantly reduced [ $^{68}\text{Ga}$ ]Ga-NOTA-Nb1053 uptake in the disseminated bone lesions, indicating the overlapping targeting epitopes of [ $^{68}\text{Ga}$ ]Ga-NOTA-Nb1053 with that of daratumumab. Furthermore, premedication with sodium maleate or fructose significantly decreased kidney retention of [ $^{68}\text{Ga}$ ]Ga-NOTA-Nb1053 and improved the diagnostic value of the probe in lymphoma models.

**Conclusion** This work successfully developed a novel CD38-targeted immunoPET imaging approach that enabled precise visualization of CD38 and diagnosis of MMs. Upon clinical translation, [ $^{68}\text{Ga}$ ]Ga-NOTA-Nb1053 immunoPET may serve as a valuable CD38-targeted molecular imaging toolbox, facilitating early diagnosis of MM and precise assessment of the therapeutic responses.

## Introduction

Multiple myeloma (MM) is a hematological neoplasm of B cell lineage and is characterized by uniform overexpression of CD38 [1]. Daratumumab is a monoclonal antibody (mAb) targeting CD38 and has been approved for treating patients with either newly diagnosed or relapsed/refractory MMs [2]. Several factors synergistically dictate the efficacy of daratumumab, predominantly the CD38 expression levels [3]. Besides efficiently selecting patients before the onset of CD38-targeted therapies, precisely monitoring the therapeutic responses is equally important. At the present stage, flow cytometry examination of the biopsied samples is the only way to detect the CD38 expression. However, the biopsy is invasive and limited to assess the localized myeloma lesion. Moreover, current imaging methods are less robust in detecting and quantifying minimal residual disease (MRD) [4]. To this end, there is an urgent need to

develop sensitive new techniques that can noninvasively annotate CD38 expression and describe the response depth following CD38-targeted therapies.

Immuno-positron emission tomography (immunoPET) is a paradigm-shifting molecular imaging technique that can detect human malignancies, inflammatory diseases, and immune cells [5-7]. We have developed several immunoPET probes to facilitate the early diagnosis of advanced thyroid cancer and melanoma, among others [8-11]. In the meanwhile, daratumumab has been radiolabeled for imaging CD38 in preclinical MM models [12, 13], and more recently in clinical trials [14, 15]. However, the size of mAb (150 kDa) exceeds the cutoff of glomerular filtration (60 kDa) and therefore long-lived radionuclides such as  $^{89}\text{Zr}$  ( $t_{1/2} = 78.4$  h) and  $^{64}\text{Cu}$  ( $t_{1/2} = 12.7$  h) are needed to match the lengthy circulation. Besides, repeated imaging at several time-points is obligatory to yield optimal tumor-to-background ratio (TBR). From a clinical perspective, a feasible and reproducible imaging protocol needs to be established before carrying out mAb-based immunoPET imaging. It should not be neglected that unbound  $^{89}\text{Zr}$  is a bone-seeking radiometal [9], potentially compromising the accuracy of  $^{89}\text{Zr}$ -mAb in detecting disseminated MMs [14]. In this setting, molecular imaging probes with enhanced stability and smaller size would be more beneficial for clinical translation.

Owing to their smaller size (~15 kDa) and excellent antigen recognition ability, Nanobody (a trade name of Ablynx) or single-domain antibody (sdAb) has emerged as alternatives for molecular imaging [16]. Nanobody-derived immunoPET probes targeting human epidermal growth factor receptor 2 and programmed death ligand-1 have been successfully translated to the bedside [17, 18]. Over the past years, we have been focusing on investigating the catalytic functions of CD38 and developing CD38-targeted therapeutics [19-21]. In this process, we produced a CD38-targeting sdAb (i.e., Nb1053) that shares similar binding epitopes with the daratumumab [19], indicating that Nb1053-based molecular imaging probes may select patients suitable for daratumumab treatment. In this work, we aim to develop [ $^{68}\text{Ga}$ ]Ga-NOTA-Nb1053 and characterize the diagnostic value of [ $^{68}\text{Ga}$ ]Ga-NOTA-Nb1053 immunoPET in preclinical MM and lymphoma models.

## Materials And Methods

### Cell lines and flow cytometry

A few solid cancer cell lines (i.e., A375, A549, BCPAP, TPC-1, FTC-133, and THJ-16T) and hematological neoplasm cell lines (i.e., Daudi and MM.1S) were used in the work. All the cell lines were cultured under the recommended protocols. To detect the expression of CD38 on the surface of the included cell lines, flow cytometry was carried out following the protocol we previously described [9, 10]. Briefly,  $1 \times 10^6$  cells for each sample were collected and washed with cold phosphate-buffered saline (PBS, HyClone). The washed cells were re-suspended in flow cytometry staining buffer (Invitrogen) and incubated with a FITC-conjugated anti-human CD38 monoclonal antibody (Catalog#: 11-0388-42; eBioscience™) on ice for 45 min in dark, with a concentration of 0.25  $\mu\text{g}/\text{mL}$  or 0.5  $\mu\text{g}/\text{mL}$ , respectively. The samples were washed

again, resuspended in PBS, and analyzed with a CytoFLEX Flow Cytometer (Beckman Coulter, Inc). The results were analyzed with the FlowJo software (FlowJo LLC).

### **Production and characterization of radiolabeled sdAbs**

Production details and sequences of Nb1053 and NbGFP are described in our previous report [19] and in the work by Kubala et al [22]. Briefly, a llama was immunized with recombinant human CD38 (residue 45–300) and phage display technology was used to obtain the positive clones. The sequences of Nb1053, a positive clone, and NbGFP, a sdAb against the green fluorescent protein (GFP) serving as the negative control, were cloned into pET28a. The proteins with His<sub>6</sub>-tags were expressed in *E.coli* BL21 (DE3) and purified by affinity chromatography (Ni-Excel, GE Cytiva) and anion-exchange chromatography (HiTrap Q, GE Cytiva). To facilitate <sup>68</sup>Ga-labeling, the sdAbs were first conjugated with a bifunctional chelator 2-S-(4-Isothiocyanatobenzyl)-1,4,7-triazacyclononane-1,4,7-triacetic acid (*p*-SCN-Bn-NOTA; Macrocyclics). Briefly, 1 mg of sdAb (i.e., Nb1053 or NbGFP) in the PBS was prepared and the pH of the sdAb solution was adjusted to 9.0–10 by adding 0.1 M Na<sub>2</sub>CO<sub>3</sub> buffer. The chelator was freshly dissolved in dimethyl sulfoxide (DMSO) and immediately added to the sdAb solution with a chelator/sdAb ratio of 10:1. The reaction was incubated at room temperature for two hours, followed by purification with equilibrated PD-10 desalting columns (GE Healthcare) and concentration with Amicon™ Ultra Centrifugal Filter (10 kDa, Merck). The concentrated antibody solution was stored at 4 °C and was stable for at least 3 months.

For radiolabeling, 370–555 MBq of freshly eluted <sup>68</sup>Ga in 0.1 M hydrogen chloride (pH = 1) was mixed with equal volume of 1 M sodium acetate (pH = 5). The radiometal solution with a final volume of 2 mL (pH = 4.0–4.5) was added to 100–200 µg of NOTA-sdAb, followed by incubation of the mixture at 37 °C for 5–10 min under constant shaking (600 rpm). The final radiopharmaceuticals were purified using equilibrated PD-10 columns and the radiochemical purity was assessed by instant thin-layer chromatography (iTLC; Eckert & Ziegler Radiopharma Inc.) and high-performance liquid chromatography (HPLC, Agilent). Analytical HPLC has been performed with Agilent 1260 Infinity II with a Superdex™ 75 Increase 5/15 GL column (5 × 153–158 mm<sup>2</sup>, ~ 9 µm). Absorbance was detected at 280 nm and radiation with an in-line Packard A-100 detector. To assess the immunoreactivity of [<sup>68</sup>Ga]Ga-NOTA-Nb1053, 200–250 µCi of the probe in 200 µL of PBS was added to 50 µg of recombinant human CD38 protein (CD8-H5224; ACROBiosystems). The binding reaction was incubated for 15 min followed by HPLC analysis with PBS as the mobile phase at a flow rate of 0.5 mL/min.

### **Subcutaneous and disseminated multiple myeloma models**

All animal experimental procedures and protocols had been approved by the Institutional Animal Care and Use Committee (Renji Hospital, School of Medicine, Shanghai Jiao Tong University). To establish subcutaneous and disseminated MM models, the well-recognized MM cell line MM.1S was used [23]. For subcutaneous models, 2 × 10<sup>6</sup> MM.1S cells were suspended in sterile PBS and matrigel matrix (Corning) with a ratio of 1:1 and then injected into the right posterior flanks of female NOD-

Prkdc<sup>em26Cd52</sup>Il2rg<sup>em26Cd22</sup>/Nju mice (NCG, 4–5 weeks; GemPharmatech). For orthotopic MM models,  $0.5 \times 10^6$  MM.1S cells in 100  $\mu$ L of sterile PBS were injected *via* tail vein to the NCG mice. The subcutaneous and orthotopic models were ready for PET imaging three weeks after tumor cell inoculation. For the subcutaneous models, the average diameter of the tumor was 0.6–1.0 cm before imaging.

### **PET imaging and data analyses**

On average,  $9.05 \pm 3.47$  MBq ( $n = 16$ ) of [<sup>68</sup>Ga]Ga-NOTA-Nb1053 or  $3.31 \pm 0.654$  MBq ( $n = 5$ ) of [<sup>68</sup>Ga]Ga-NOTA-NbGFP was administered to the tumor-bearing NCG mice. For mAb premedication studies, daratumumab (1 mg/mouse; Janssen Biotech, Inc.) was administered to the disseminated MM models ten hours before [<sup>68</sup>Ga]Ga-NOTA-Nb1053 injection. For one specific disseminated MM model, daratumumab was administered two days before injection of the radiotracer. On average,  $5.56 \pm 0.179$  MBq ( $n = 5$ ) of <sup>18</sup>F-fluorodeoxyglucose (<sup>18</sup>F-FDG) was injected *via* tail vein to the fasted mice, and images were acquired one hour after tracer injection. <sup>18</sup>F-FDG PET imaging was performed according to a previously reported protocol with minor modification [9]. In the one-hour uptake phase, the fasted mice were warmed and kept awake to reduce brown tissue uptake and minimize unexpected deaths.

To test whether lysine and/or gelofusine could reduce kidney accumulation of [<sup>68</sup>Ga]Ga-NOTA-Nb1053, nine normal ICR mice (Shanghai SLAC Laboratory Animal Co., Ltd) were randomly divided into three groups: control group, gelofusine group (150 mg/Kg), and gelofusine + lysine group (150 mg/Kg of gelofusine and 400 mg/Kg of lysine, respectively). The injected activity for each group was  $15.5 \pm 0.50$  MBq ( $n = 3$ ),  $11.41 \pm 0.60$  MBq ( $n = 3$ ), and  $10.87 \pm 0.96$  MBq ( $n = 3$ ), respectively. The effect of mannitol, fructose, and sodium maleate on the kidney accumulation of [<sup>68</sup>Ga]Ga-NOTA-Nb1053 was further evaluated and compared with another group of control mice [24]. The average injected dose of [<sup>68</sup>Ga]Ga-NOTA-Nb1053 in these four groups was  $2.640 \pm 0.6511$  MBq ( $n = 3$ ),  $1.092 \pm 0.2312$  MBq ( $n = 4$ ),  $5.542 \pm 1.509$  MBq ( $n = 4$ ), and  $6.717 \pm 1.211$  MBq ( $n = 3$ ), respectively. The detailed injection information was summarized in Table S1.

The mice were anesthetized and placed in the prone position in the scanning bed. PET/CT data were acquired in sequence with an IRIS PET/CT system (Inviscan Imaging Systems). PET data were reconstructed using a non-scatter-corrected 3D-ordered subset expectation optimization/maximum a posteriori (OSEM3D/MAP) algorithm and subsequently analyzed using the OsiriX Lite software (Pixmeo SARL) and the Inveon Research Workplace (Siemens Preclinical Solutions).

### **Biodistribution and histopathological studies**

After termination of the immunoPET imaging studies, the mice were sacrificed and samples including blood were collected and weighed. The radioactivity of the samples was counted using an automated  $\gamma$ -counter (Perkin-Elmer) and the uptake of the radiotracers in different organs/tissues was calculated and given as percent of injected dose per gram of tissue (%ID/g, mean  $\pm$  SD).

To rigorously evaluate the tumor burden in the MM models, both subcutaneous tumors and bone tissues (humerus, femur, and tibia) of representative NCG mice were fixed in 10% neutral buffered formalin and used for hematoxylin and eosin (H&E) and immunohistochemistry (IHC) staining. The bone tissues were decalcified in ethylene diamine tetraacetic acid and then processed in a similar way to the subcutaneous tumor samples. Sections of 10  $\mu\text{m}$  were cut and stained for H&E, CD38 (10818-R128, SinoBiological, and ab183326, Abcam), and CD138 (MCA2459GA, BIO-RAD) using standard protocols. To detect the location of the pre-injected daratumumab (also served as the primary antibody), a horseradish peroxidase (HRP)-labeled rabbit anti-human IgG H&L (ab6759, Abcam) was used as the secondary antibody.

## Statistical analysis

Statistical analysis was performed using the GraphPad software. Data are presented as means  $\pm$  SD as stated in the figure legends.  $P < 0.05$  was considered statistically significant.

# Results

## Flow cytometry screening

We screened a range of cancer cell lines by flow cytometry and found that CD38 was positively expressed on two hematological malignancy cell lines (MM.1S and Daudi) (Supplemental Fig. 1). In line with the result from previous work [25], positive expression of CD38 was also found on the A549 cell line. Besides, CD38 was negative on four thyroid cancer cell lines (BCPAP, TPC-1, FTC-133, and THJ-16T) and a melanoma cell line (A375).

## Development and characterization of radiotracers

To design immunoPET imaging probes, two sdAbs targeting either GFP or human CD38 were first modified with the chelator NOTA and then radiolabeled with  $^{68}\text{Ga}$  ( $t_{1/2} = 1.1$  h). The non-decay corrected radiolabeling yield of [ $^{68}\text{Ga}$ ]Ga-NOTA-Nb1053 and [ $^{68}\text{Ga}$ ]Ga-NOTA-NbGFP was  $47.84 \pm 12.2\%$  ( $n = 8$ ) and  $26.43\%$  ( $n = 1$ ), respectively. The radiochemical purities of the two radiotracers were  $> 99\%$  and remained  $> 99\%$  in the saline in three hours (Supplemental Fig. 2). The *in vivo* stability of these two tracers was tested at different time-point post-injection. The results showed that both the tracers were intact at 30 min and 1 h in blood and urine (data not shown). The stability of [ $^{68}\text{Ga}$ ]Ga-NOTA-Nb1053 meets translational requirements because PET imaging with  $^{68}\text{Ga}$ -labeled tracers usually finishes within two hours. As shown by HPLC analysis (Fig. 1), more than 95% of [ $^{68}\text{Ga}$ ]Ga-NOTA-Nb1053 complexed with its target protein CD38 and migrated rapidly than the standalone [ $^{68}\text{Ga}$ ]Ga-NOTA-Nb1053 in the size exclusion chromatography column. The antibody and radioactivity retention time of [ $^{68}\text{Ga}$ ]Ga-NOTA-Nb1053 were 3.506 min and 3.872 min, respectively (Fig. 1a, b). In comparison, the corresponding retention time of [ $^{68}\text{Ga}$ ]Ga-NOTA-Nb1053 incubated with an excess of the extracellular domain of CD38 were 2.646 min and 2.806 min, respectively (Fig. 1c, d). These results together indicated the excellent stability and immunoreactivity of the developed [ $^{68}\text{Ga}$ ]Ga-NOTA-Nb1053, warranting subsequent *in vivo* imaging studies.

## **[<sup>68</sup>Ga]Ga-NOTA-Nb1053 immunoPET imaging of subcutaneous multiple myelomas**

The diagnostic value of [<sup>68</sup>Ga]Ga-NOTA-Nb1053 immunoPET was first interrogated in mice bearing subcutaneous MM.1S xenografts. [<sup>68</sup>Ga]Ga-NOTA-Nb1053 rapidly accumulated in the tumors with excellent TBR at 1 h post-injection (Fig. 2a). In general, the probe underwent rapid renal clearance, accompanied by moderate hepatobiliary clearance. Region of interest (ROI) analysis of the PET data showed an average tumor uptake of  $1.76 \pm 0.305$  (n = 5) in terms of %ID/g. A comparable liver uptake ( $2.2 \pm 0.16\%$ ID/g, n = 5) and a significantly higher kidney uptake ( $39.46 \pm 11.77\%$ ID/g, n = 5) was derived from the analysis (Fig. 2b). In comparison, uptake in the bone and muscle was exceptionally low, leading to a tumor-to-muscle ratio of 10.90 and a tumor-to-bone ratio of 5.79. Subsequent biodistribution study confirmed the highest uptake in the kidney ( $187 \pm 43.0\%$ ID/g, n = 5), followed by the uptake in the liver ( $4.77 \pm 0.197\%$ ID/g, n = 5) and tumor ( $3.02 \pm 0.509\%$ ID/g, n = 5) (Fig. 2c). Staining of the resected tumor tissue showed prominent membrane expression of CD38 on MM.1S tumor cells (Fig. 2d, e). CD138 is another biomarker for MM and positive staining of CD138 was also observed on the tumor tissue, confirming the plasmacytic differentiation of the MM.1S cell line (Fig. 2e). The histopathological staining results matched well with the above imaging data and together indicated the good tumor-targeting affinity of [<sup>68</sup>Ga]Ga-NOTA-Nb1053. The sharp delineation of MM.1S tumors by [<sup>68</sup>Ga]Ga-NOTA-Nb1053 prompted us to compare its diagnostic value with other nonspecific imaging agents.

## **[<sup>68</sup>Ga]Ga-NOTA-NbGFP immunoPET and <sup>18</sup>F-FDG PET imaging of subcutaneous multiple myelomas**

ImmunoPET imaging with [<sup>68</sup>Ga]Ga-NOTA-NbGFP, a nonspecific radiotracer targeting GFP, failed to delineate the subcutaneous MM.1S tumors (Fig. 3a). When compared to [<sup>68</sup>Ga]Ga-NOTA-Nb1053, [<sup>68</sup>Ga]Ga-NOTA-NbGFP had significantly lower tumor uptake ( $0.343 \pm 0.072\%$ ID/g vs.  $1.76 \pm 0.305\%$ ID/g,  $P < 0.0001$ ) and higher liver uptake ( $5.98 \pm 1.29\%$ ID/g vs.  $2.2 \pm 0.158\%$ ID/g,  $P = 0.0002$ ). However, the two radiotracers had comparable kidney accumulation based on the ROI analysis ( $40.3 \pm 8.39\%$ ID/g, n = 5 vs.  $39.5 \pm 11.8\%$ ID/g, n = 5;  $P = 0.9022$ ; Fig. 3b). Prominent renal and hepatobiliary clearance of [<sup>68</sup>Ga]Ga-NOTA-NbGFP was further supported by the biodistribution study (Supplemental Fig. 3). After analyzing the biodistribution data, we confirmed that [<sup>68</sup>Ga]Ga-NOTA-NbGFP had significantly lower tumor uptake than [<sup>68</sup>Ga]Ga-NOTA-Nb1053 ( $0.289 \pm 0.0437\%$ ID/g, n = 4 vs.  $3.02 \pm 0.509\%$ ID/g, n = 5;  $P < 0.0001$ ). Consistently, kidney had the highest accumulation of [<sup>68</sup>Ga]Ga-NOTA-Nb1053 ( $35.4 \pm 18.5\%$ ID/g, n = 4), followed by the uptake in the liver ( $9.10 \pm 0.805\%$ ID/g, n = 4). The kidney uptake disparities of the two radiotracers on the biodistribution data was unknown. We assume that differences in injection dose and sbAb sequences are potential reasons.

To further show the merits of [<sup>68</sup>Ga]Ga-NOTA-Nb1053, <sup>18</sup>F-FDG PET imaging was carried out in another five subcutaneous MM.1S models. Despite its ability in delineating the tumors with an average uptake of  $3.82 \pm 0.766\%$ ID/g (n = 5; Fig. 3c), <sup>18</sup>F-FDG had high nonspecific uptake in the normal tissues or organs (Fig. 3d), such as bone marrow, muscle, and brown tissue. The high nonspecific uptake of <sup>18</sup>F-FDG resulted in a lower tumor-to-muscle ratio of 1.25 and a tumor-to-bone ratio of 0.39. From a diagnostic perspective, the high bone uptake of <sup>18</sup>F-FDG unavoidably impedes accurate diagnosis of disseminated

MM diseases. Taken together, [<sup>68</sup>Ga]Ga-NOTA-Nb1053 showed distinct advantages over [<sup>68</sup>Ga]Ga-NOTA-NbGFP and <sup>18</sup>F-FDG in diagnosing subcutaneous MMs.

### **[<sup>68</sup>Ga]Ga-NOTA-Nb1053 immunoPET imaging of disseminated multiple myelomas**

Next, we assessed the potency of [<sup>68</sup>Ga]Ga-NOTA-Nb1053 immunoPET in imaging disseminated (i.e., orthotopic) MMs. [<sup>68</sup>Ga]Ga-NOTA-Nb1053 immunoPET readily delineated all the bone lesions three weeks (data not shown) and four weeks after the tumor cell inoculation. Specifically, [<sup>68</sup>Ga]Ga-NOTA-Nb1053 immunoPET precisely visualized MM lesions in the skull, humeri, sternum, scapulae, vertebrae, femora, tibiae, and pelvis bones (Fig. 4a, b). Quantitative analysis showed that uptake of [<sup>68</sup>Ga]Ga-NOTA-Nb1053 in the humerus, femur, and tibia was  $2.250 \pm 0.866\%$ ID/g,  $2.625 \pm 0.877\%$ ID/g, and  $2.325 \pm 0.932\%$ ID/g (n = 4), respectively. Premedication with the full-length mAb daratumumab substantially reduced [<sup>68</sup>Ga]Ga-NOTA-Nb1053 uptake in these involved bones (Fig. 4c, d), with the corresponding uptake were  $0.839 \pm 0.243\%$ ID/g,  $0.712 \pm 0.305\%$ ID/g, and  $0.580 \pm 0.288\%$ ID/g (n = 3), respectively. Interestingly, one subcutaneous MM.1S model developed spontaneous metastases. In this case, [<sup>68</sup>Ga]Ga-NOTA-Nb1053 immunoPET visualized all the involved bones in addition to the subcutaneous MM.1S tumor. With an interval of two days, daratumumab premedication substantially reduced the retention of [<sup>68</sup>Ga]Ga-NOTA-Nb1053 in the subcutaneous and disseminated MM lesions (Supplemental Fig. 4). Quantitative analysis showed that premedication using daratumumab increased liver uptake of [<sup>68</sup>Ga]Ga-NOTA-Nb1053, but the increase was not statistically significant (Supplemental Fig. 5). These data demonstrated the efficacy and merits of [<sup>68</sup>Ga]Ga-NOTA-Nb1053 in imaging disseminated MMs.

H&E staining of a representative humerus showed diffuse bone marrow involvement by plasma cells (Fig. 5a). As illustrated by the IHC staining results (Fig. 5b), the CD138 and CD38 double-positive plasma cells diffusely replaced the normal bone marrow. We then asked if the pre-injected daratumumab dispersed into the bone marrow and bound to the plasma cells. As expected, staining of a representative humerus of the daratumumab treatment group showed bone marrow involvement by massive plasma cells (Fig. 5c). Deposition of daratumumab-bound plasma cells was found in the osteoepiphysis and diaphysis of the humerus (Fig. 5d), indicating the deposition of daratumumab in the disseminated MMs. These results together demonstrated the successful establishment of the orthotopic MM.1S models and the superior accuracy of [<sup>68</sup>Ga]Ga-NOTA-Nb1053 immunoPET in delineating disseminated MMs.

### **Strategies reducing kidney accumulation of [<sup>68</sup>Ga]Ga-NOTA-Nb1053**

Although high kidney accumulation of a radioligand may not affect the diagnostic decision, it will cause unexpected nephrotoxicity when the radioligand is used for therapeutic purposes. A recent clinical trial has shown the therapeutic potential of <sup>131</sup>I-labeled sdAb [26]. The high kidney accumulation of [<sup>68</sup>Ga]Ga-NOTA-Nb1053 largely resided in the renal cortex (Fig. 6a), which may still appear when swapping <sup>68</sup>Ga with therapeutic radionuclides (e.g., <sup>177</sup>Lu). We explored several strategies to circumvent this potential drawback at the diagnostic stage (Supplemental Table 1). It has been reported that co-injection of gelofusine and lysine could reduce kidney uptake [27]. We tested but failed to observe such an effect in

our case (Supplemental Fig. 6). The osmotic diuretic mannitol also did not affect the overall and kidney uptake of [<sup>68</sup>Ga]Ga-NOTA-Nb1053 (Fig. 6b). We further tested the potential role of sodium maleate and fructose in manipulating the kidney uptake, both of which can decrease ATP production in the kidneys. Administration of these two compounds substantially reduced kidney uptake of [<sup>68</sup>Ga]Ga-NOTA-Nb1053 (Fig. 6c, d). A higher dose of maleate (14.4 mg/mouse compared to 9.6 mg/mouse) more robustly reduced kidney accumulation of [<sup>68</sup>Ga]Ga-NOTA-Nb1053 (Supplemental Fig. 7) but was associated with severe toxicity.

As revealed by the ROI analysis (Fig. 7a), the kidney uptake in the fructose intervention group and the maleate intervention group was  $26.150 \pm 7.948\%ID/g$  ( $n = 4$ ) and  $18.725 \pm 11.092\%ID/g$  ( $n = 4$ ), respectively. The uptake in the above two groups was significantly lower than that in the control group ( $39.100 \pm 1.153\%ID/g$ ,  $n = 3$ ) or the mannitol intervention group ( $39.467 \pm 5.918\%ID/g$ ,  $n = 3$ ). Moreover, sodium maleate decreased the kidney accumulation of the radiotracer more prominently than fructose ( $P = 0.012$ ). These results were further consolidated by the biodistribution studies (Fig. 7b). Intraperitoneal injection of fructose slightly prolonged the circulation of [<sup>68</sup>Ga]Ga-NOTA-Nb1053 and the retention of the radiotracer in several organs such as the lung, but the increase was not statistically significant compared to other groups. These data suggest that sodium maleate is preferred when it is necessary to reduce the undesired kidney uptake of radiometal-labeled Nb1053.

### **Optimized [<sup>68</sup>Ga]Ga-NOTA-Nb1053 immunoPET imaging of lymphomas**

A previous study has indicated the potency of CD38-targeted immunoPET in imaging lymphomas [28]. Our flow cytometry results also revealed positive CD38 expression on Daudi cells. With the above information in hand, we explored the diagnostic utility of [<sup>68</sup>Ga]Ga-NOTA-Nb1053 immunoPET in lymphoma xenografts in the context of maleate premedication. As shown in Supplemental Fig. 8a, [<sup>68</sup>Ga]Ga-NOTA-Nb1053 immunoPET readily delineated subcutaneous Daudi tumors. The overall distribution and uptake features of [<sup>68</sup>Ga]Ga-NOTA-Nb1053 was similar to that observed in the subcutaneous MM.1S models. Owing to the maleate premedication, the kidney uptake reduced substantially in the Daudi models when compared to that in the subcutaneous MM.1S models, with the value dropped from  $39.460 \pm 11.770\%ID/g$  ( $n = 5$ ) to  $14.167 \pm 4.609\%ID/g$  ( $n = 3$ ) (Supplemental Fig. 8b). The effect of maleate premedication on the kidney uptake of [<sup>68</sup>Ga]Ga-NOTA-Nb1053 was further confirmed by comparing the biodistribution data of the two groups (Supplemental Fig. 8c), where the kidney uptake decreased more than 3.5 times ( $52.9 \pm 28.9\%ID/g$  [ $n = 3$ ] vs.  $187 \pm 43.0\%ID/g$  [ $n = 5$ ],  $P = 0.0032$ ). Although tumor uptake of [<sup>68</sup>Ga]Ga-NOTA-Nb1053 was higher in the Daudi tumors than in the MM.1S tumors based on the biodistribution data ( $3.43 \pm 1.61\%ID/g$  [ $n = 3$ ] vs.  $3.02 \pm 0.509\%ID/g$  [ $n = 5$ ]), the increase was not statistically significant ( $P = 0.5954$ ). Finally, IHC staining further revealed intense CD38 and CD138 expression on the Daudi tumor (Supplemental Fig. 8d, e), visually more intensive than the staining intensity of the subcutaneous MM.1S tumor (Fig. 2e). These results together demonstrated the value of [<sup>68</sup>Ga]Ga-NOTA-Nb1053 immunoPET in diagnosing lymphomas and the potency of maleate premedication in optimizing the TBR.

## Discussion

Currently, whole-body low-dose computed tomography is preferred for detecting lytic bone lesions and magnetic resonance imaging is the method of choice for detecting bone marrow involvement by MM [29].  $^{18}\text{F}$ -FDG PET is also used to detect MRD [30, 31], but its value is limited when a low hexokinase-2 expression or high background uptake occurs [32]. With the development and future clinical translation of  $^{68}\text{Ga}$ ]Ga-NOTA-Nb1053, clinicians can detect MM at earlier stages.  $^{68}\text{Ga}$ ]Ga-NOTA-Nb1053 immunoPET may detect multiple myeloma-involved bones without obvious bone destruction, allowing for efficient patient stratification and selection. Additionally, this novel imaging approach can help assess treatment response and disease recurrence in a CD38-dependent manner. Different from traditional mAb-based probes, the sdAb-derived  $^{68}\text{Ga}$ ]Ga-NOTA-Nb1053 will permit same-day imaging with higher TBR. This improvement eliminates the concern of nonspecific bone accumulation in the course of tedious  $^{89}\text{Zr}$ -mAb immunoPET imaging [9, 14]. The spleen may not capture sdAbs due to the lack of Fc fragments. Therefore, another merit of  $^{68}\text{Ga}$ ]Ga-NOTA-Nb1053 is that there is no need to administrate unlabeled Nb1053 to saturate the extremely high spleen uptake. As a companion diagnostic tool,  $^{68}\text{Ga}$ ]Ga-NOTA-Nb1053 immunoPET may optimize CD38-targeted radioimmunotherapy [33, 34]. Considering that CD38 is an alternative tumor marker for other hematological malignancies [28], it is rational to expand the application scenarios of  $^{68}\text{Ga}$ ]Ga-NOTA-Nb1053. Indeed,  $^{68}\text{Ga}$ ]Ga-NOTA-Nb1053 immunoPET realized the precise diagnosis of lymphomas in the current work, it may also aid in the diagnosis and stratification of solid tumors [25, 35].

As seen from the data,  $^{68}\text{Ga}$ ]Ga-NOTA-Nb1053 was largely excreted from the urinary system, reabsorbed in the proximal tubule cells, and degraded by the lysosomes. The metabolic mechanism resulted in the accumulation of the radioactive catabolites in the renal cortex (Fig. 6 and Supplemental Fig. 6). Megalin is an endocytic receptor in the proximal tubule cells and is involved in the reabsorption of proteins and peptides [36]. The plasma expander gelofusine and the positively charged basic amino acid lysine are the targets of megalin. Co-injection of gelofusine and lysine inhibited renal uptake of  $^{99\text{m}}\text{Tc}$ -labeled sdAb [37]. However, gelofusine and lysine failed to reduce the kidney uptake of  $^{68}\text{Ga}$ -NOTA-Nb1053 in our study. Of the several compounds tested, sodium maleate and fructose showed a robust effect in reducing kidney accumulation of  $^{68}\text{Ga}$ ]Ga-NOTA-Nb1053, presumably by decreasing ATP production in the proximal tubule cells. These observations indicate that different mechanisms are involved in the uptake of differently radiolabeled sdAbs. This knowledge may help develop new strategies to reduce renal retention of Nb1053-derived radioligands and alleviate the nephrotoxicity. We are exploring other strategies (e.g., PEGylation) to increase the tumor uptake and reduce the kidney uptake simultaneously [38]. Besides, our unpublished data showed that  $^{18}\text{F}$ -labeled Nb1053 shifted its excretion pathway from the urinary system to the hepatobiliary system. The information is clinically relevant when radiolabeled Nb1053 is used for treatment purposes.

The treatment landscape of MM has incrementally improved in the past three decades. This success was achieved through the clinical use of proteasome inhibitors and immunomodulatory drugs, including the

daratumumab. Despite the encouraging results, 40% of MM patients responded poorly to daratumumab treatment. In this setting, [<sup>68</sup>Ga]Ga-NOTA-Nb1053 immunoPET may help visualize fluctuating CD38 expression, select patients, predict response, and monitor resistance. Since Nb1053 competes with daratumumab in binding to CD38, radiotracers binding to CD38 independently of the daratumumab (or isatuximab) will more precisely monitor the dynamic change of CD38 following the antibody therapies [39]. Although the rapid clinical translation of two mAb-based CD38-targeted immunoPET probes [14, 15], the development of immunoPET imaging technique with sdAbs is still in this infancy. We have demonstrated the feasibility of [<sup>68</sup>Ga]Ga-NOTA-Nb1053 immunoPET in imaging MMs in preclinical models. Clinical translation of this novel CD38-targeted imaging strategy is underway. Along with the progress, we and others have developed B cell maturation antigen (BCMA)-targeting chimeric antigen receptor-modified T (CAR-T) and treatment of relapsed and refractory MMs with CAR-T cell infusion resulted in a revolutionary overall response rate [40]. Therefore, alternative MM biomarkers such as BCMA and CD138 may also be leveraged in developing MM-specific molecular imaging tracers. Development and clinical translation of these state-of-the-art companion diagnostic agents will hopefully improve the clinical management of patients with MM.

To summarize, we have successfully developed [<sup>68</sup>Ga]Ga-NOTA-Nb1053 and immunoPET imaging with this radiotracer visualized MM niduses with excellent clarity and accuracy.

## Declarations

**Funding** This work was supported in part by the National Key Research and Development Program of China (Grant No. 2020YFA0909000), National Natural Science Foundation of China (Grant No. 81771858, 81830052, 81530053, 31871403, and 82001878), Shanghai Key Laboratory of Molecular Imaging (Grant No. 18DZ2260400), Shanghai Rising-Star Program (Grant No. 20QA1406100), Foundation for Basic Research of Science and Technology Project in Shenzhen (Grant No. JCYJ20190808163411340), Construction Project of Shanghai Key Laboratory of Molecular Imaging (Grant No. 18DZ2260400), and Shanghai Municipal Education Commission (Class II Plateau Disciplinary Construction Program of Medical Technology of SUMHS, 2018-2020).

**Conflict of interest** W. Wei and J. Liu are co-inventors on a provisional patent application (Application No. 202011131233.7) encompassing the technology described in this manuscript.

**Ethics approval** Not applicable

**Consent to participate** Not applicable

**Consent for publication** Not applicable

**Availability of data and material** All the raw data and materials involved in the work can be obtained from Prof. Wei upon rational request.

**Code availability** Not applicable

**Authors' contributions** W. Wei, J. Liu, and Y. J. Zhao collaboratively conceived and designed the project. C. Wang, Y. Chen, W. Wei, Q. Liu, and D. Zhang performed the experiments and wrote most of the manuscript. Y. N. Hou produced the sdAbs and contributed to the writing. S. An, Y. Zhang, and H. Zhao helped in the radiolabeling and characterization of the radiotracers. J. Hou and G. Huang provided inputs in the initial design of the project and revised the manuscript. W. Wei, J. Liu, and Y. J. Zhao supervised the study, revised, and finalized the manuscript.

## References

1. Rajkumar SV, Dimopoulos MA, Palumbo A, Blade J, Merlini G, Mateos MV, et al. International Myeloma Working Group updated criteria for the diagnosis of multiple myeloma. *Lancet Oncol.* 2014;15:e538-48. doi:10.1016/S1470-2045(14)70442-5.
2. Nooka AK, Kaufman JL, Hofmeister CC, Joseph NS, Heffner TL, Gupta VA, et al. Daratumumab in multiple myeloma. *Cancer.* 2019;125:2364-82. doi:10.1002/cncr.32065.
3. van de Donk N, Richardson PG, Malavasi F. CD38 antibodies in multiple myeloma: back to the future. *Blood.* 2018;131:13-29. doi:10.1182/blood-2017-06-740944.
4. Kumar S, Paiva B, Anderson KC, Durie B, Landgren O, Moreau P, et al. International Myeloma Working Group consensus criteria for response and minimal residual disease assessment in multiple myeloma. *Lancet Oncol.* 2016;17:e328-e46. doi:10.1016/S1470-2045(16)30206-6.
5. Wei W, Rosenkrans ZT, Liu J, Huang G, Luo QY, Cai W. ImmunoPET: Concept, Design, and Applications. *Chem Rev.* 2020;120:3787-851. doi:10.1021/acs.chemrev.9b00738.
6. Wei W, Ni D, Ehlerding EB, Luo QY, Cai W. PET Imaging of Receptor Tyrosine Kinases in Cancer. *Mol Cancer Ther.* 2018;17:1625-36. doi:10.1158/1535-7163.MCT-18-0087.
7. Wei W, Jiang D, Ehlerding EB, Luo Q, Cai W. Noninvasive PET Imaging of T cells. *Trends Cancer.* 2018;4:359-73. doi:10.1016/j.trecan.2018.03.009.
8. Wei W, Jiang D, Lee HJ, Li M, Kuttyreff CJ, Engle JW, et al. Development and characterization of CD54-targeted immunoPET imaging in solid tumors. *Eur J Nucl Med Mol Imaging.* 2020;47:2765-75. doi:10.1007/s00259-020-04784-0.
9. Wei W, Jiang D, Ehlerding EB, Barnhart TE, Yang Y, Engle JW, et al. CD146-Targeted Multimodal Image-Guided Photoimmunotherapy of Melanoma. *Adv Sci (Weinh).* 2019;6:1801237. doi:10.1002/advs.201801237.
10. Wei W, Jiang D, Rosenkrans ZT, Barnhart TE, Engle JW, Luo Q, et al. HER2-targeted multimodal imaging of anaplastic thyroid cancer. *Am J Cancer Res.* 2019;9:2413-27.
11. Wei W, Liu Q, Jiang D, Zhao H, Kuttyreff CJ, Engle JW, et al. Tissue Factor-Targeted ImmunoPET Imaging and Radioimmunotherapy of Anaplastic Thyroid Cancer. *Adv Sci (Weinh).* 2020;7:1903595. doi:10.1002/advs.201903595.

12. Caserta E, Chea J, Minnix M, Poku EK, Viola D, Vonderfecht S, et al. Copper 64-labeled daratumumab as a PET/CT imaging tracer for multiple myeloma. *Blood*. 2018;131:741-5. doi:10.1182/blood-2017-09-807263.
13. Ghai A, Maji D, Cho N, Chanswangphuwana C, Rettig M, Shen D, et al. Preclinical Development of CD38-Targeted [(89)Zr]Zr-DFO-Daratumumab for Imaging Multiple Myeloma. *J Nucl Med*. 2018;59:216-22. doi:10.2967/jnumed.117.196063.
14. Ulaner GA, Sobol NB, O'Donoghue JA, Kirov AS, Riedl CC, Min R, et al. CD38-targeted Immuno-PET of Multiple Myeloma: From Xenograft Models to First-in-Human Imaging. *Radiology*. 2020;295:606-15. doi:10.1148/radiol.2020192621.
15. Krishnan A, Adhikarla V, Poku EK, Palmer J, Chaudhry A, Biglang-Awa VE, et al. Identifying CD38+ cells in patients with multiple myeloma: first-in-human imaging using copper-64-labeled daratumumab. *Blood Adv*. 2020;4:5194-202. doi:10.1182/bloodadvances.2020002603.
16. Chakravarty R, Goel S, Cai W. Nanobody: the "magic bullet" for molecular imaging? *Theranostics*. 2014;4:386-98. doi:10.7150/thno.8006.
17. Xing Y, Chand G, Liu C, Cook GJR, O'Doherty J, Zhao L, et al. Early Phase I Study of a (99m)Tc-Labeled Anti-Programmed Death Ligand-1 (PD-L1) Single-Domain Antibody in SPECT/CT Assessment of PD-L1 Expression in Non-Small Cell Lung Cancer. *J Nucl Med*. 2019;60:1213-20. doi:10.2967/jnumed.118.224170.
18. Keyaerts M, Xavier C, Heemskerk J, Devoogdt N, Everaert H, Ackaert C, et al. Phase I Study of 68Ga-HER2-Nanobody for PET/CT Assessment of HER2 Expression in Breast Carcinoma. *J Nucl Med*. 2016;57:27-33. doi:10.2967/jnumed.115.162024.
19. Li T, Qi S, Unger M, Hou YN, Deng QW, Liu J, et al. Immuno-targeting the multifunctional CD38 using nanobody. *Sci Rep*. 2016;6:27055. doi:10.1038/srep27055.
20. An N, Hou YN, Zhang QX, Li T, Zhang QL, Fang C, et al. Anti-Multiple Myeloma Activity of Nanobody-Based Anti-CD38 Chimeric Antigen Receptor T Cells. *Mol Pharm*. 2018;15:4577-88. doi:10.1021/acs.molpharmaceut.8b00584.
21. Deng QW, Zhang J, Li T, He WM, Fang L, Lee HC, et al. The transferrin receptor CD71 regulates type II CD38, revealing tight topological compartmentalization of intracellular cyclic ADP-ribose production. *J Biol Chem*. 2019;294:15293-303. doi:10.1074/jbc.RA119.010010.
22. Kubala MH, Kovtun O, Alexandrov K, Collins BM. Structural and thermodynamic analysis of the GFP:GFP-nanobody complex. *Protein Sci*. 2010;19:2389-401. doi:10.1002/pro.519.
23. Greenstein S, Krett NL, Kurosawa Y, Ma C, Chauhan D, Hideshima T, et al. Characterization of the MM.1 human multiple myeloma (MM) cell lines: a model system to elucidate the characteristics, behavior, and signaling of steroid-sensitive and -resistant MM cells. *Exp Hematol*. 2003;31:271-82. doi:10.1016/s0301-472x(03)00023-7.
24. Altai M, Garousi J, Rinne SS, Schulga A, Deyev S, Vorobyeva A. On the prevention of kidney uptake of radiolabeled DARPins. *EJNMMI Res*. 2020;10:7. doi:10.1186/s13550-020-0599-1.

25. Ehlerding EB, England CG, Jiang D, Graves SA, Kang L, Lacognata S, et al. CD38 as a PET Imaging Target in Lung Cancer. *Mol Pharm*. 2017;14:2400-6. doi:10.1021/acs.molpharmaceut.7b00298.
26. D'Huyvetter M, De Vos J, Caveliers V, Vaneycken I, Heemskerk J, Duhoux FP, et al. Phase I trial of (131)I-GMIB-Anti-HER2-VHH1, a new promising candidate for HER2-targeted radionuclide therapy in breast cancer patients. *J Nucl Med*. 2020;jnumed.120.255679. doi:10.2967/jnumed.120.255679.
27. Chatalic KL, Veldhoven-Zweistra J, Bolkestein M, Hoeben S, Koning GA, Boerman OC, et al. A Novel (1)(1)(1)In-Labeled Anti-Prostate-Specific Membrane Antigen Nanobody for Targeted SPECT/CT Imaging of Prostate Cancer. *J Nucl Med*. 2015;56:1094-9. doi:10.2967/jnumed.115.156729.
28. Kang L, Jiang D, England CG, Barnhart TE, Yu B, Rosenkrans ZT, et al. ImmunoPET imaging of CD38 in murine lymphoma models using (89)Zr-labeled daratumumab. *Eur J Nucl Med Mol Imaging*. 2018;45:1372-81. doi:10.1007/s00259-018-3941-3.
29. Zamagni E, Tacchetti P, Cavo M. Imaging in multiple myeloma: How? When? *Blood*. 2019;133:644-51. doi:10.1182/blood-2018-08-825356.
30. Cavo M, Terpos E, Nanni C, Moreau P, Lentzsch S, Zweegman S, et al. Role of (18)F-FDG PET/CT in the diagnosis and management of multiple myeloma and other plasma cell disorders: a consensus statement by the International Myeloma Working Group. *Lancet Oncol*. 2017;18:e206-e17. doi:10.1016/S1470-2045(17)30189-4.
31. Kumar S, Glazebrook KN, Broski SM. Fludeoxyglucose F 18 PET/Computed Tomography Evaluation of Therapeutic Response in Multiple Myeloma. *PET Clin*. 2019;14:391-403. doi:10.1016/j.cpet.2019.03.006.
32. Rasche L, Angtuaco E, McDonald JE, Buros A, Stein C, Pawlyn C, et al. Low expression of hexokinase-2 is associated with false-negative FDG-positron emission tomography in multiple myeloma. *Blood*. 2017;130:30-4. doi:10.1182/blood-2017-03-774422.
33. Bailly C, Chalopin B, Gouard S, Carlier T, Saëc PR-L, Marionneau-Lambot S, et al. ImmunoPET in Multiple Myeloma—What? So What? Now What? *Cancers (Basel)*. 2020;12:1467. doi:10.3390/cancers12061467.
34. Minnix M, Adhikarla V, Caserta E, Poku E, Rockne R, Shively JE, et al. Comparison of CD38 targeted alpha- vs beta-radionuclide therapy of disseminated multiple myeloma in an animal model. *J Nucl Med*. 2020. doi:10.2967/jnumed.120.251983.
35. Li S, England CG, Ehlerding EB, Kuttyreff CJ, Engle JW, Jiang D, et al. ImmunoPET imaging of CD38 expression in hepatocellular carcinoma using 64Cu-labeled daratumumab. *Am J Transl Res*. 2019;11:6007-15.
36. Nielsen R, Christensen EI, Birn H. Megalin and cubilin in proximal tubule protein reabsorption: from experimental models to human disease. *Kidney Int*. 2016;89:58-67. doi:10.1016/j.kint.2015.11.007.
37. Gainkam LO, Caveliers V, Devoogdt N, Vanhove C, Xavier C, Boerman O, et al. Localization, mechanism and reduction of renal retention of technetium-99m labeled epidermal growth factor receptor-specific nanobody in mice. *Contrast Media Mol Imaging*. 2011;6:85-92. doi:10.1002/cmml.408.

38. Rashidian M, Ingram JR, Dougan M, Dongre A, Whang KA, LeGall C, et al. Predicting the response to CTLA-4 blockade by longitudinal noninvasive monitoring of CD8 T cells. *J Exp Med*. 2017;214:2243-55. doi:10.1084/jem.20161950.
39. Fumey W, Koenigsdorf J, Kunick V, Menzel S, Schutze K, Unger M, et al. Nanobodies effectively modulate the enzymatic activity of CD38 and allow specific imaging of CD38(+) tumors in mouse models in vivo. *Sci Rep*. 2017;7:14289. doi:10.1038/s41598-017-14112-6.
40. Xu J, Chen LJ, Yang SS, Sun Y, Wu W, Liu YF, et al. Exploratory trial of a biepitopic CAR T-targeting B cell maturation antigen in relapsed/refractory multiple myeloma. *Proc Natl Acad Sci U S A*. 2019;116:9543-51. doi:10.1073/pnas.1819745116.

## Figures

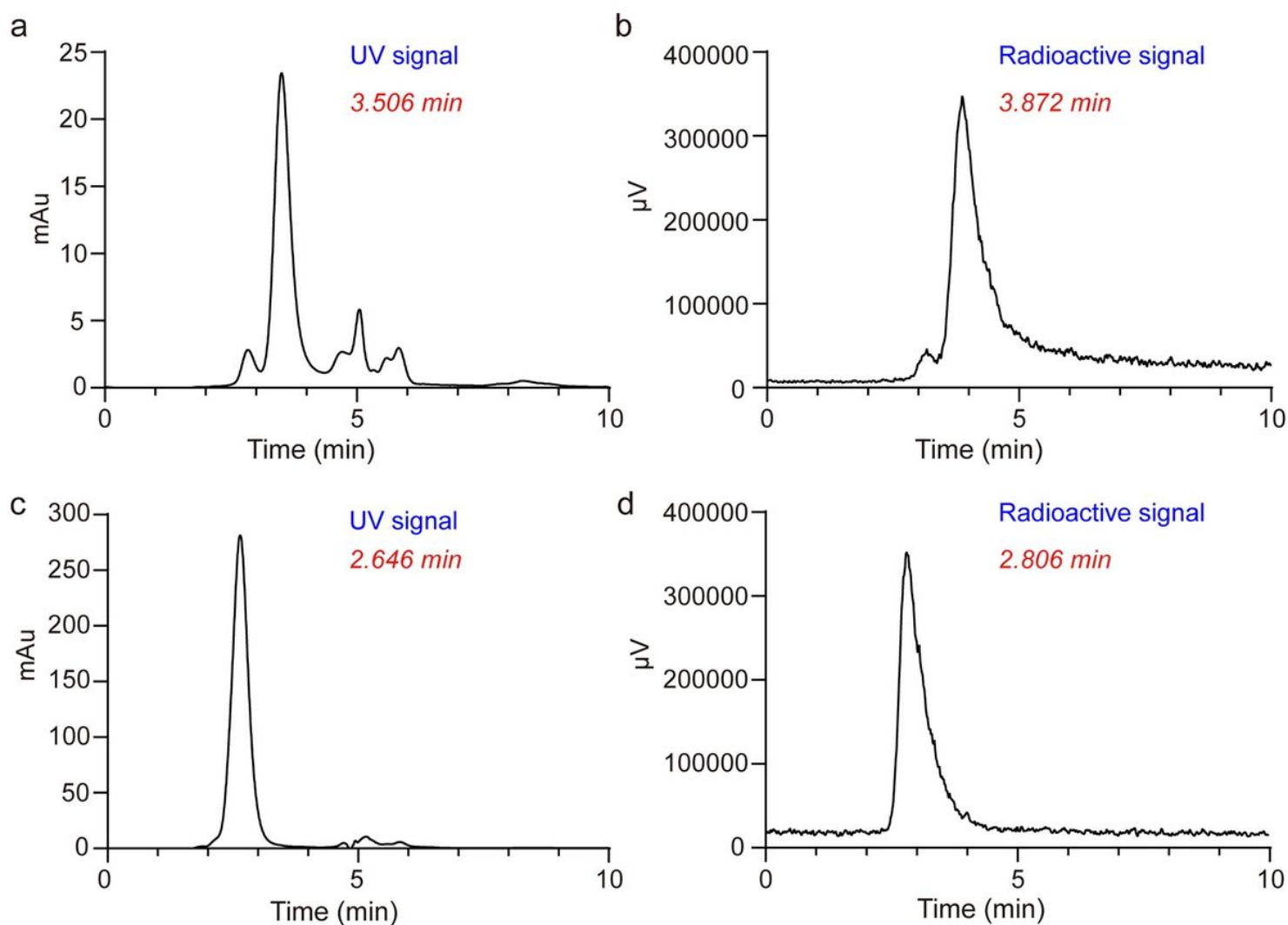


**Figure 1**

Characterization of  $[^{68}\text{Ga}]\text{Ga-NOTA-Nb1053}$  by high-performance liquid chromatography (HPLC). a, b HPLC analysis of integrity (UV signal) and radiochemical purity (radioactive signal) of  $[^{68}\text{Ga}]\text{Ga-NOTA-Nb1053}$ .

Nb1053. c, d HPLC analysis of equal dose of  $[^{68}\text{Ga}]\text{Ga-NOTA-Nb1053}$  incubated with 50  $\mu\text{g}$  of recombinant human CD38 protein.

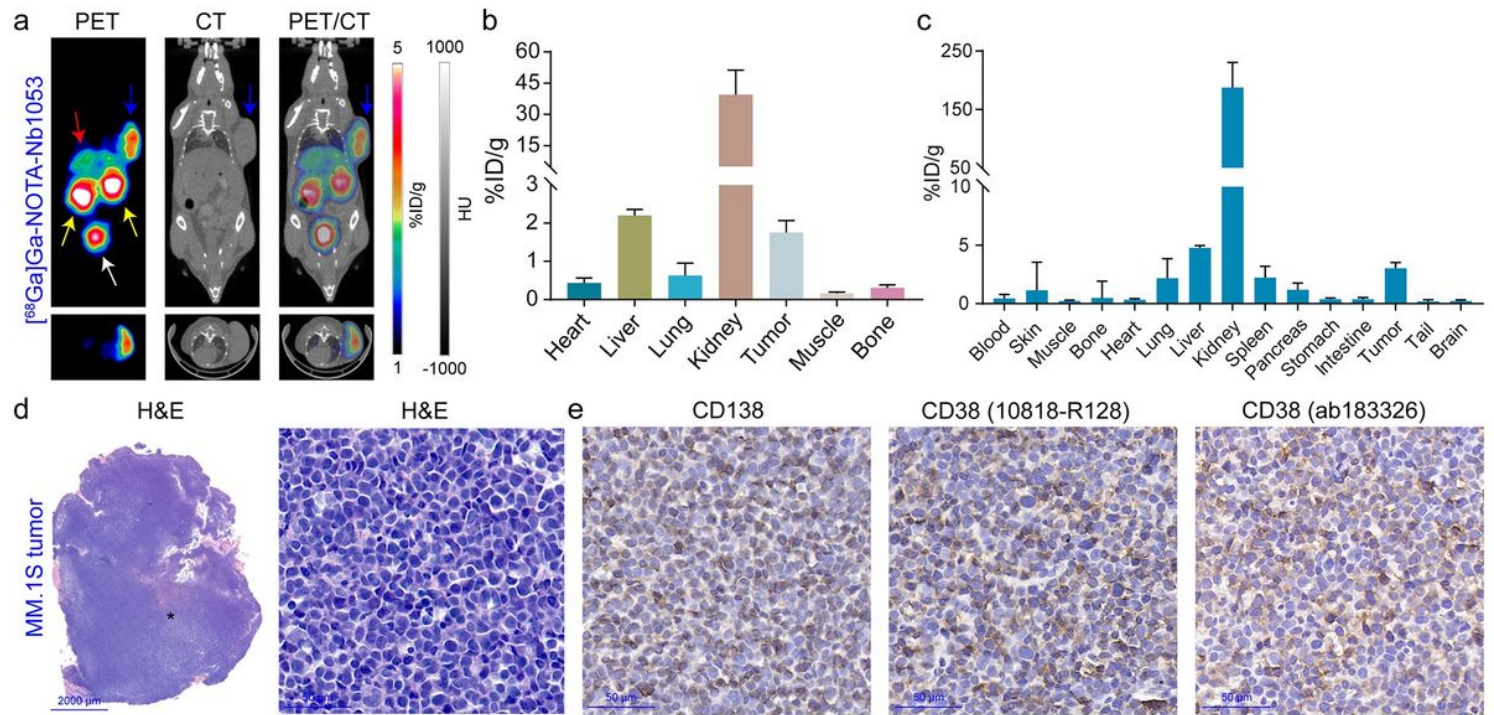


**Figure 2**

$[^{68}\text{Ga}]\text{Ga-NOTA-Nb1053}$  immunoPET imaging of subcutaneous multiple myeloma. a  $[^{68}\text{Ga}]\text{Ga-NOTA-Nb1053}$  immunoPET imaging of subcutaneous multiple myeloma. Coronal (up panel) and transversal (down panel) images showed a clear delineation of the tumor (blue arrow). The liver, kidney, and bladder were indicated by the red arrow, yellow arrows, and white arrow, respectively. b Region of interest (ROI) analysis of the immunoPET data (n = 5). c Biodistribution data showing the overall distribution of the tracer in the blood circulation, major organs, or tissues (n = 5). d Macroscopic hematoxylin and eosin (H&E) staining of the resected MM.1S tumor (left) and microscopic staining of the area indicated by the black asterisk (right). e Immunohistochemistry staining of CD138 (left) and CD38 (middle and right) of the resected MM.1S tumor. Two different clones (10818-R128, SinoBiological, and ab183326, Abcam) were used to stain and cross-validate the CD38 expression. ROI and biodistribution data were presented in terms of Mean  $\pm$  SD.

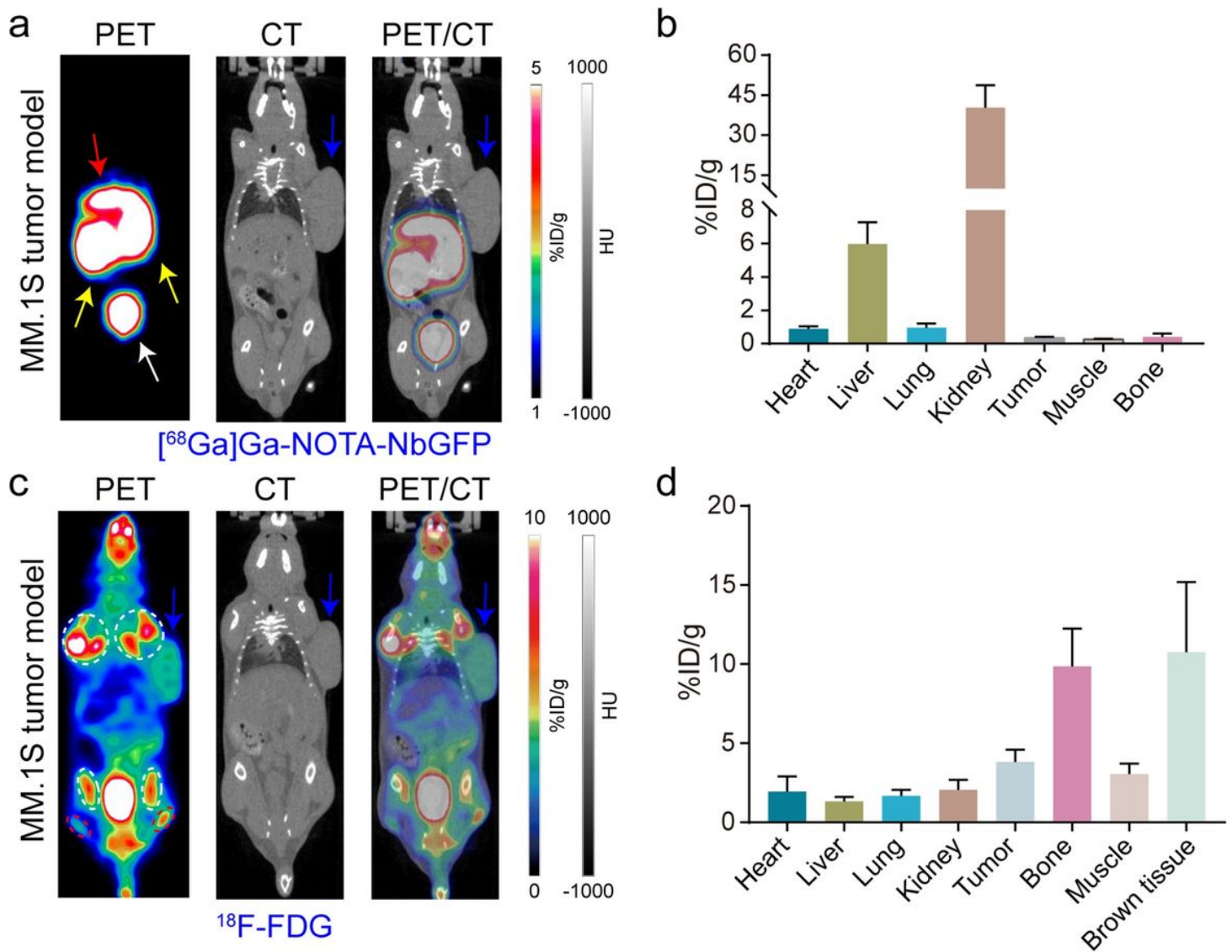


**Figure 3**

Nonspecific nuclear medicine imaging of subcutaneous multiple myelomas. a [<sup>68</sup>Ga]Ga-NOTA-NbGFP immunoPET imaging of subcutaneous multiple myelomas. Coronal images showed no visual uptake of [<sup>68</sup>Ga]Ga-NOTA-NbGFP in the tumor (blue arrow). The liver, kidney, and bladder were indicated by the red arrow, yellow arrows, and white arrow, respectively. b Region of interest (ROI) analysis of the immunoPET data (n = 5). c <sup>18</sup>F-FDG PET imaging of subcutaneous multiple myelomas. Nonspecific uptake of <sup>18</sup>F-FDG in the bones (white dashed circles), muscles (red dashed circles), and brown adipose tissue compromised the specificity of <sup>18</sup>F-FDG in imaging the tumor (blue arrow). d Region of interest analysis of the PET data (n = 5). ROI and biodistribution data were presented in terms of Mean ± SD.

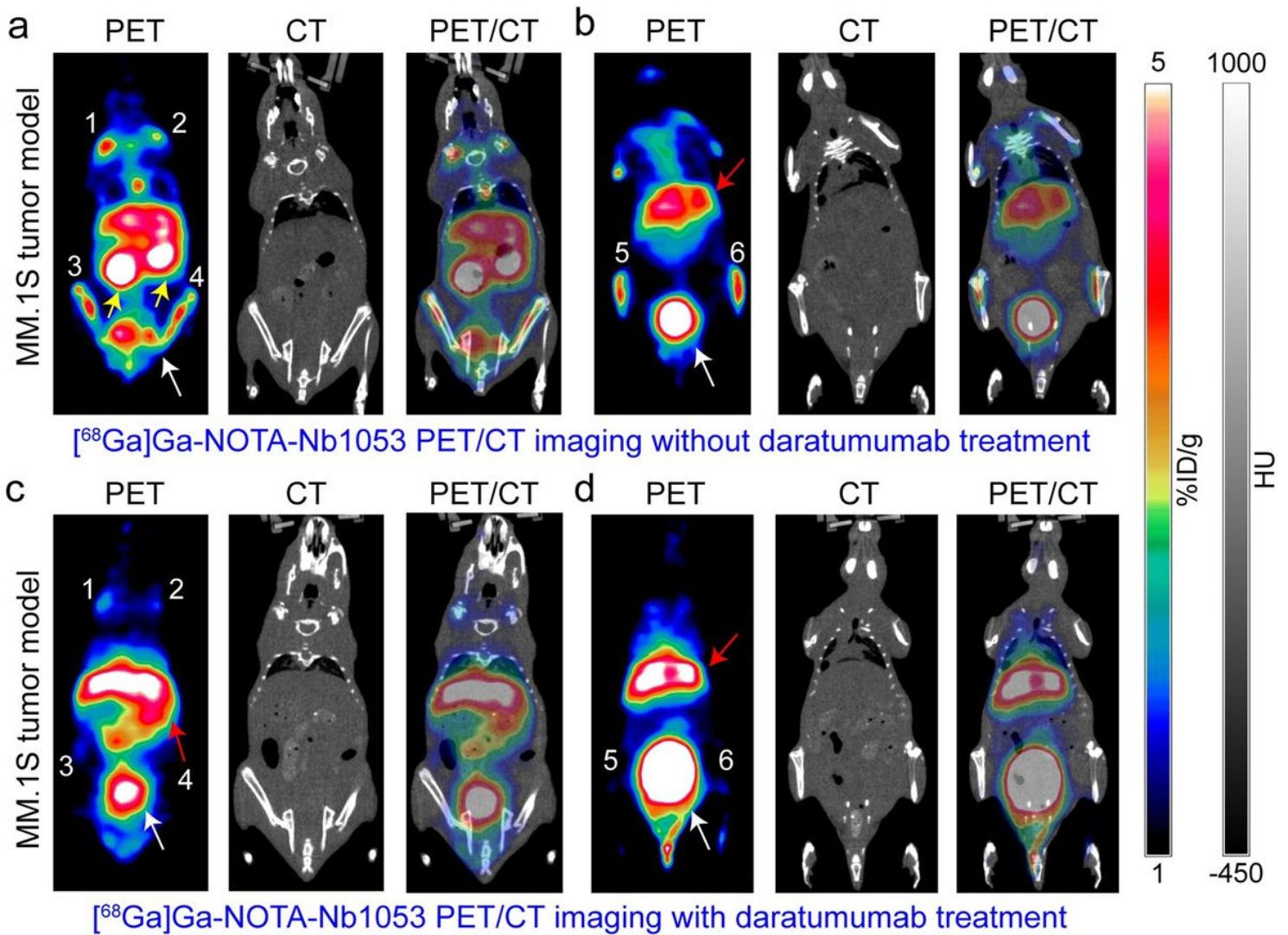


**Figure 4**

$[^{68}\text{Ga}]\text{Ga-NOTA-Nb1053}$  immunoPET imaging of disseminated multiple myeloma. a, b Coronal immunoPET/CT images showed prominent  $[^{68}\text{Ga}]\text{Ga-NOTA-Nb1053}$  uptake in the MM.1S-involved humeri (1 and 2), femora (3 and 4), and tibiae (5 and 6). c, d Coronal immunoPET/CT images showed decreased  $[^{68}\text{Ga}]\text{Ga-NOTA-Nb1053}$  uptake in the above-mentioned bones following daratumumab premedication. The liver, kidney, and bladder were indicated by the red arrow, yellow arrow, and white arrow, respectively.

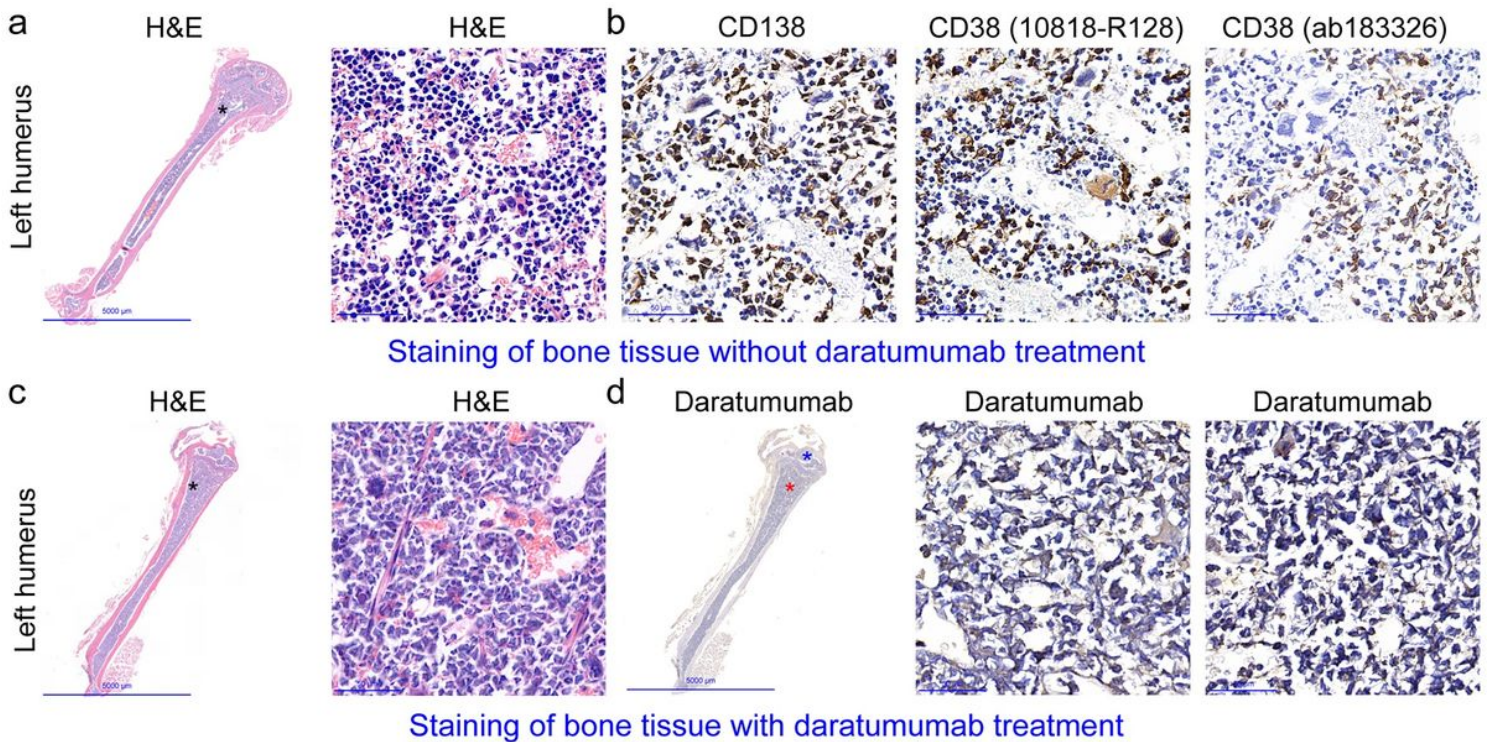


**Figure 5**

Hematoxylin and eosin (H&E) and immunohistochemistry (IHC) staining studies. a Macroscopic (left) and microscopic (black asterisk, right) H&E staining of a representative humerus. b IHC staining of the same humerus showed bone marrow involvement by CD138 and CD38 double-positive plasma cells. A monoclonal antibody (10818-R128, SinoBiological) was used to stain CD38 expression and another monoclonal antibody (ab183326, Abcam) was used to confirm the expression. c H&E staining of a representative humerus of the daratumumab treatment group (left). d For the IHC staining, the pre-loaded daratumumab served as the primary antibody. Positive staining of daratumumab was found in the osteoepiphysis (blue asterisk, middle) and diaphysis (red asterisk, right).

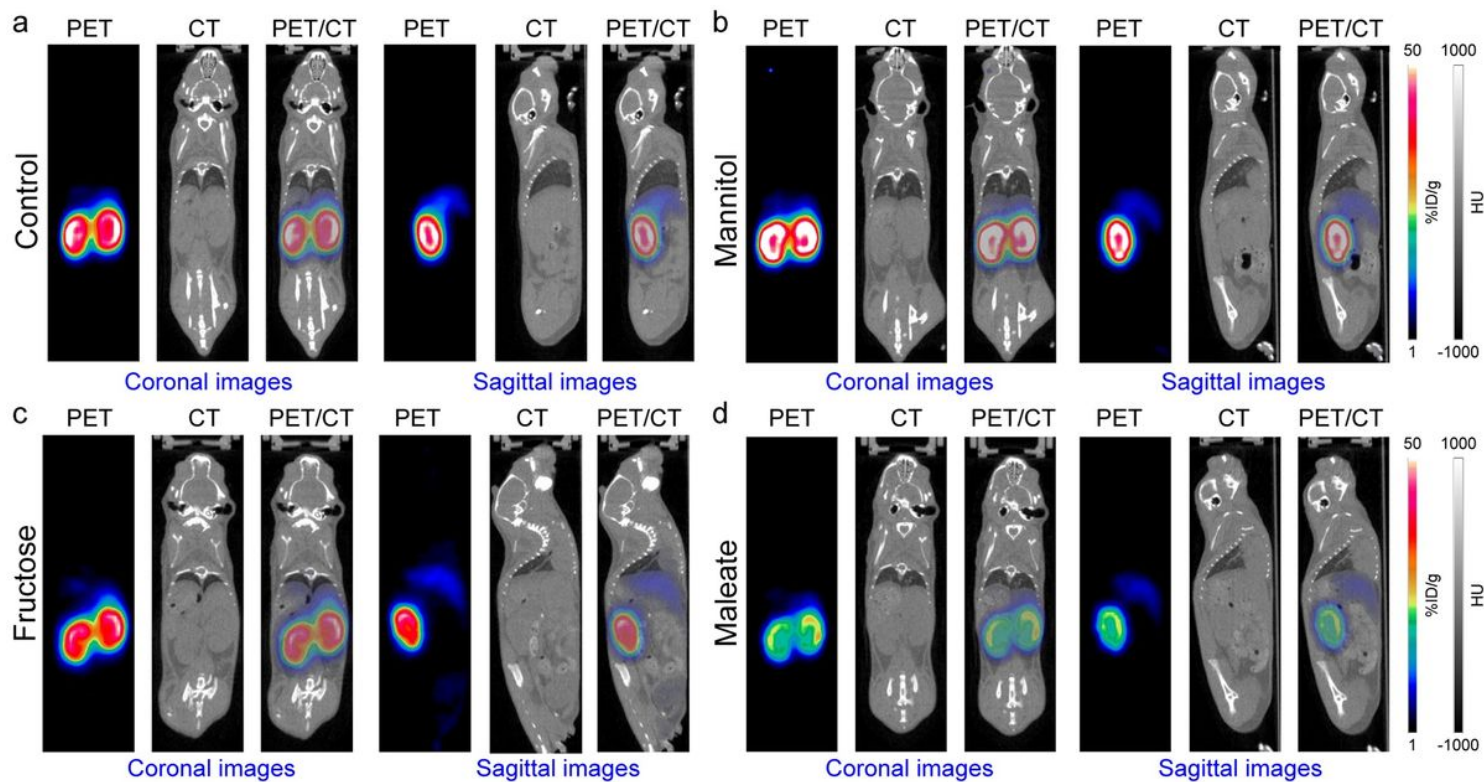


**Figure 6**

Strategies reducing kidney accumulation of  $[^{68}\text{Ga}]\text{Ga-NOTA-Nb1053}$  in normal ICR mice. Representative coronal and sagittal  $[^{68}\text{Ga}]\text{Ga-NOTA-Nb1053}$  immunoPET/CT images of mice in control group (a), mannitol intervention group (b), fructose intervention group (c), and sodium maleate intervention group (d).

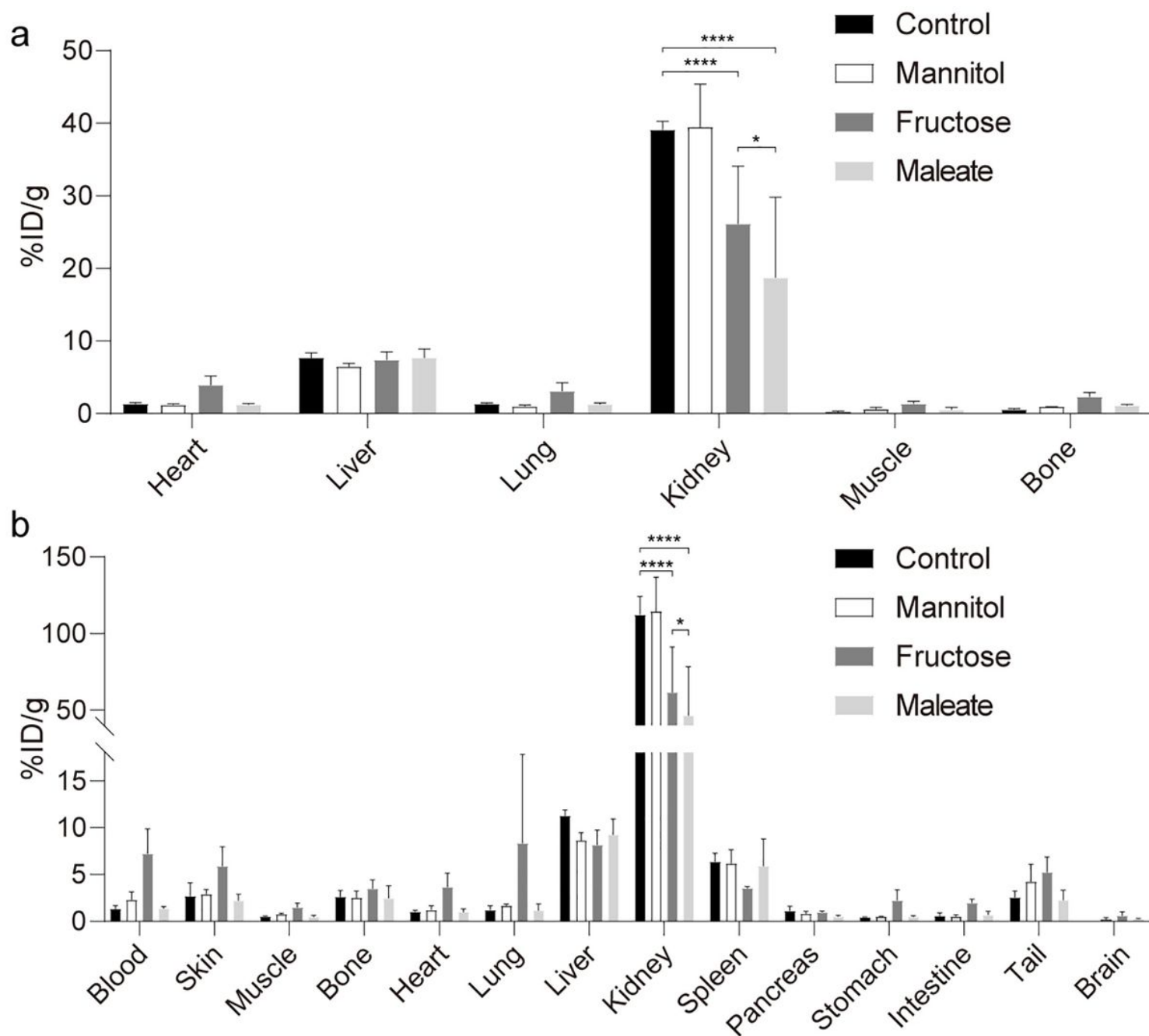


**Figure 7**

Quantitative analyses of the [68Ga]Ga-NOTA-Nb1053 immunoPET imaging and biodistribution data. a Region of interest analysis of immunoPET imaging data. \*\*\*\*:  $P < 0.0001$ . \*:  $P = 0.0120$ . b Ex vivo biodistribution data showing detailed uptake of [68Ga]Ga-NOTA-Nb1053 in the blood, major organs, and tissues. \*\*\*\*:  $P < 0.0001$ . \*:  $P = 0.0199$ . Data were presented in terms of Mean  $\pm$  SD.

## Supplementary Files

This is a list of supplementary files associated with this preprint. Click to download.

- [Supplementalmaterials.docx](#)